Nanoscale

PAPER

View Article Online
View Journal | View Issue

Cite this: *Nanoscale*, 2023, **15**, 17861

Coal waste-derived synthesis of yellow oxidized graphene quantum dots with highly specific superoxide dismutase activity: characterization, kinetics, and biological studies†

Tushar Das, [a] Subrata Das, *[a] Prakash Kumar,[b] Betty C.A.[c,d] and Debabrata Mandal *[b]

The disintegration of coal-based precursors for the scalable production of nanozymes relies on the fate of solvothermal pyrolysis. Herein, we report a novel economic and scalable strategy to fabricate yellow luminescent graphene quantum dots (YGQDs) by remediating unburnt coal waste (CW). The YGQDs (size: 7–8 nm; M.W: 3157.9 Da) were produced using *in situ* "anion-radical" assisted bond cleavage in water (within 8 h; at 121 °C) with yields of ~87%. The presence of exposed surface and edge groups, such as COOH, C–O–C, and O–H, as structural defects accounted for its high fluorescence with ε_{max} ~530 nm at pH 7. Besides, these defects also acted as radical stabilizers, demonstrating prominent anti-oxidative activity of ~4.5-fold higher than standard ascorbic acid (AA). In addition, the YGQDs showed high biocompatibility towards mammalian cells, with 500 μM of treatment dose showing <15% cell death. The YGQDs demonstrated specific superoxide dismutase (SOD) activity wherein 15 μM YGQDs equalled the activity of 1-unit biological SOD (bSOD), measured using the pyrogallol assay. The K_m for YGQDs was ~10-fold higher than that for bSOD. However, the YGQDs retained their SOD activity in harsh conditions like high temperatures or denaturing reactions, where the activity of bSOD is completely lost. The binding affinity of YGQDs for superoxide ions, measured from isothermal calorimetry (ITC) studies, was only 10-fold lower than that of bSOD (K_d of 586 nM *vs.* 57.3 nM). Further, the pre-treatment of YGQDs (~10–25 μM) increased the cell survivability to >75–90% in three cell lines during ROS-mediated cell death, with the highest survivability being shown for C6-cells. Next, the ROS-induced apoptosis in C6-cells (model for neurodegenerative diseases study), wherein YGQDs uptake was confirmed by confocal microscopy, showed ~5-fold apoptosis alleviation with only 5 μM pretreatment. The YGQDs also restored the expression of pro-inflammatory Th1 cytokines (TNF-α, IFN-γ, IL-6) and anti-inflammatory Th2 cytokines (IL-10) to their basal levels, with a net >3-fold change observed. This further explains the molecular mechanism for the antioxidant property of YGQDs. The high specific SOD activity associated with YGQDs may provide the cheapest alternative source for producing large-scale SOD-based nanozymes that can treat various oxidative stress-linked disorders/diseases.

Received 24th August 2023,
Accepted 9th October 2023

DOI: 10.1039/d3nr04259f

rsc.li/nanoscale

Introduction

Graphene quantum dots (GQDs) represent an arsenal class of fragmented zero-band gap material with a size range usually below ~15 nm. The diverse physio-chemical properties from its quantum Hall and confinement effects prospect its applications in nano-biotechnology-driven research.[1] Chemically, GQDs can be produced from a variety of biogenic precursors like glucose, graphitic derivatives, carbon nanotubes (CNT), carbon nanofibers (CNF), and other carbon-rich sources either through "top–down" or "bottom–up" routes.[2–9] However, using such manifested precursors is often bounded by their expensiveness and operational instabilities, resulting in high manu-

[a]*Department of Chemistry, National Institute of Technology Patna, Bihar 800005, India. E-mail: subrataorgchem@gmail.com, subratad@nitp.ac.in*
[b]*Department of Biotechnology, National Institute of Pharmaceutical Education and Research Hajipur, Vaishali 844102, India. E-mail: debabrataman@gmail.com*
[c]*Chemistry Division, Bhabha Atomic Research Centre, Mumbai 400085, India*
[d]*Homi Bhabha National Institute, Mumbai 400085, India*

†Electronic supplementary information (ESI) available: Pretreatment of coal; synthesis of GO from CW; general instrumentation; HR-TEM sample preparation and EDS map of YGQDs and GO; UV-vis spectra of GO and pH-dependent photophysical studies of YGQDs; cytotoxic studies and hemolytic assay; H_2O_2 degradation activity; monitoring YGQDs internalization in C-6 cells using confocal microscopy; degradation of H_2O_2 free radical by YGQDs; MTT assay color changes for LPS + YGQDs; ELISA picture representing color intensities for MDA level estimation. See DOI: https://doi.org/10.1039/d3nr04259f

facturing costs and lower practical yields. Moreover, precision techniques, such as critical water treatment,[10] pulse laser ablation in liquid,[11] and material deflagration methods,[12] require complicated inert assemblies for production. A considerable switch to sustainable precursors with facile methodologies might provide a profitable and scalable alternative to solve such limitations.[13] In this regard, stable GQDs were produced from trifling varieties of coal through simplistic methods, offering good aqueous dispersibility and providing newer developments in coal-based research.[14–17] The natural process of thermal cracking that entirely relies on carbonization phenomena arising from the differences in the atomic composition of materials can be a promising approach to produce GQDs.[18] Besides, the abundance of stacked aliphatic domains and different oxygenated compositions of coal allow additional sites for oxidative cleavage.[19] In addition, the logarithmic increase in the rapid utilization of coal-based energy has led to an alarming rise in different environmental pollutions.[20–22] Hence, we envisioned our strategy of remediating harmful coal remains from nature by converting them into less toxic GQDs with a nano-enzymatic activity that can be used for alleviating free radical-induced oxidative disease.

Biologically, the inherent properties of GQDs, like controllable tunability in photoluminescence, high loading capacity, and radiation capture ability, make them suitable for photodynamic therapies, biosensors, bio-imaging, and drug carriers.[23] Moreover, the abundance of surface functional groups like COOH, OH, C=C, and C–O–C serve as catalytic sites, similar to that in enzymes, to carry out various bio-transformation reactions.[24] Unlike other inorganic nanomaterials, GQDs offer much higher cellular biocompatibility, for which they are used as a therapy replacement for natural enzymes.[25,26] In addition, GQDs provide a much cheaper production cost, better shelf-life, and reusability than natural enzymatic supplements.[27] In this regard, Sun *et al.* used SOD/CAT-mediated anti-oxidative and protective oxidized GQDs against alcohol-intoxicated cell lines.[28] Kim *et al.* showed the blood–brain barrier permeability of GQDs, and its specific interactions with α-synuclein can prevent its accumulation and aggregation during Parkinson's disease progression.[29] Hu *et al.* used GQDs/semiconducting polymer nanocomposites as a synergistic photothermal and nano-enzymatic agent for better tumor therapy by combining the intrinsic peroxidase activity of GQDs and temperature-sensitive production of singlet oxygen ($^1O_2$).[30] So far, most of the nanoenzymatic roles of GQDs reported are linked to its natural peroxidase-like behavior. For example Xin *et al.* synthesized histidine-functionalized GQDs/hemin complex with high peroxidase turnover, with the hemin group acting as natural peroxidase mimics.[31] Sun *et al.* illustrated the catalytic mechanism of peroxidase-like activity in GQDs by the selective activation and deactivation of different functional groups, wherein the surface-exposed C=O groups served as active sites.[32] Nirala *et al.* reported an electrochemical preparation of GQDs having natural peroxidase activity that were further used as natural colorimetric probes to detect trace levels of glucose and H_2O_2.[33] Amongst the different bio-properties, GQDs with inherent radical scavenging activity (RSA) are most widely studied due to its association with different therapies to counter elevated levels of oxidative stress (OS) under a diseased state. In this regard, the explicit report of Wang *et al.* showed that hydrogen bond donation and radical adduct formation ability of GQDs initiated by different surface speciation of oxygenated functional groups are the main reason for the quenching of free radicals.[34] Nilewski *et al.* showed that polyethylene glycol-functionalized GQDs can rescue murine endothelioma cells from severe H_2O_2 stress through SOD-linked activity.[35] Krunić *et al.* explored the anti-oxidative property of GQDs against oxidative and nitrative damages in SH-SY5Y neuroblastoma cells generated through sodium nitroprusside, with GQDs acting as non-selective anti-oxidants and iron chelators, with no enzymatic activity.[36] More interestingly, Wang *et al.* showed that upon halogen doping, GQDs shows a switch between its anti- and pro-oxidant behavior with good antibacterial effect mediated through generation ($^1O_2$).[37] Although multiple attempts are made to use GQDs-like enzyme mimics to treat various diseases/disorders associated with stress, its exact treatment mechanism and administrative dose for human applications is yet to be resolved. We strongly believe that even before switching to *in vivo* models, determining the dose-dependent RSA roles of such nanozymes through *ex vivo* studies will allow for fabricating much more cost-effective and precision-based formulations with lower cellular accumulation toxicities.

Current neuro-epidemiology suggests that 61% of the global mortality rate increase is due to different neurological disorders originating from the imbalance of molecular oxygen.[38,39] Perhaps almost all neurological disorders are activated by *in situ* elevated levels of reactive radical species that cause oxidative harm to both growing and mature neural cells, leading to their progression.[40,41] Ascertained by its harmful health effects, notable interest in nano-based antioxidants has shown prolific results in down-regulating the spread of tissue, protein, and DNA damages when supplemented.[42,43] Generally, inherent detoxification enzymes like superoxide dismutase (SOD), catalase (CAT), and glutathione peroxidase (GPx) act in tandem to counter these superoxide radical anions and hydrogen peroxides ($O_2^{\bullet-}$ and H_2O_2) to protect O_2 and H_2O in biological systems.[44] However, irreversible enzymatic damage resulting from a prolonged disorder/disease state requires enzymatic supplements for compensating such a loss. Till now, therapeutic replacements for natural enzymes have been quite challenging due to their high instability, low immunogenicity, and low cellular diffusibility, alongwith very low circulation half-lives. Therefore, nanozymes from non-biological sources like QDs, GQDs, and inorganic materials are considered an alternative due to their lower production cost and high scalability, besides being highly active and stable in harsh environments wherein biological enzymes become entirely inactive.

This is the first report wherein a simple fabrication strategy is reported for the large-scale production of YGQDs by CW

remediation interceded through the generation of *in situ* anion radicals directly in water. The presence of different oxygenated functional groups (like COOH, OH, and C–O–C) as surface and edge defects in YGQDs showed the stabilization of free radicals, both in *ex vivo* and *in vitro*, in a dose-dependent order. More importantly, the RSA in YGQDs was associated with its high specific SOD activity. Having demonstrated its excellent stability, the binding affinity towards $O_2^{\bullet-}$ (K_d ~586 nM) and high biocompatibility, the YGQDs were envisioned for mitigating ROS under *ex vivo* conditions. Optimal results showed amongst the different cell lines studied; YGQDs showed the highest survivability/reversal of C6-cells (~90%) from severe ROS. Furthermore, the complete normalization of different pro- and anti-inflammatory cytokines levels explains the plausible anti-apoptotic and cell survivability mechanism of YGQDs in C6-cells alongwith its time-dependent cytosolic and nuclear localization. A brief overview of the entire work is illustrated in Scheme 1. The present results emphasize an easy and cost-effective fabrication of YGQDs by remediating CW intended to countering $O_2^{\bullet-}$-driven neuronal stress.

Results

Preparation and characterization of GO and YGQDs

We first began with the synthesis of GO from a large molecular fragment of CW (isolation process mentioned in Fig. S1, ESI†), based on a safer methodology of improved Hummers method,[45] using a mixture of concentrated orthophosphoric acid and sulfuric acid ($V_{H_3PO_4} : V_{H_2SO_4}$ = 4 : 6 v/v) and potassium permanganate ($KMnO_4$ ~6 eq.) as the oxidant. The presence of disorders and small crystallizable domains in CW allowed for faster exfoliation and the formation of surface and edge defects. The fabrication of YGQDs was done using a simplified method of *in situ* generation of anion radical ($NaO_2^{\bullet-}$)-assisted bond cleavage in water.[46] The present method exempts the use of commercial radicals that suffer instability and requires special handling; hence, the *in situ* generation of radicals was preferred for synthesis.[47] The effective concentration of H_2O_2 and NaOH was determined to be 3 : 2 (mmol) for converting 100 mg GO efficiently to YGQDs, with practical yields reaching ~87.4%. Further, the purification of the formed YGQDs was

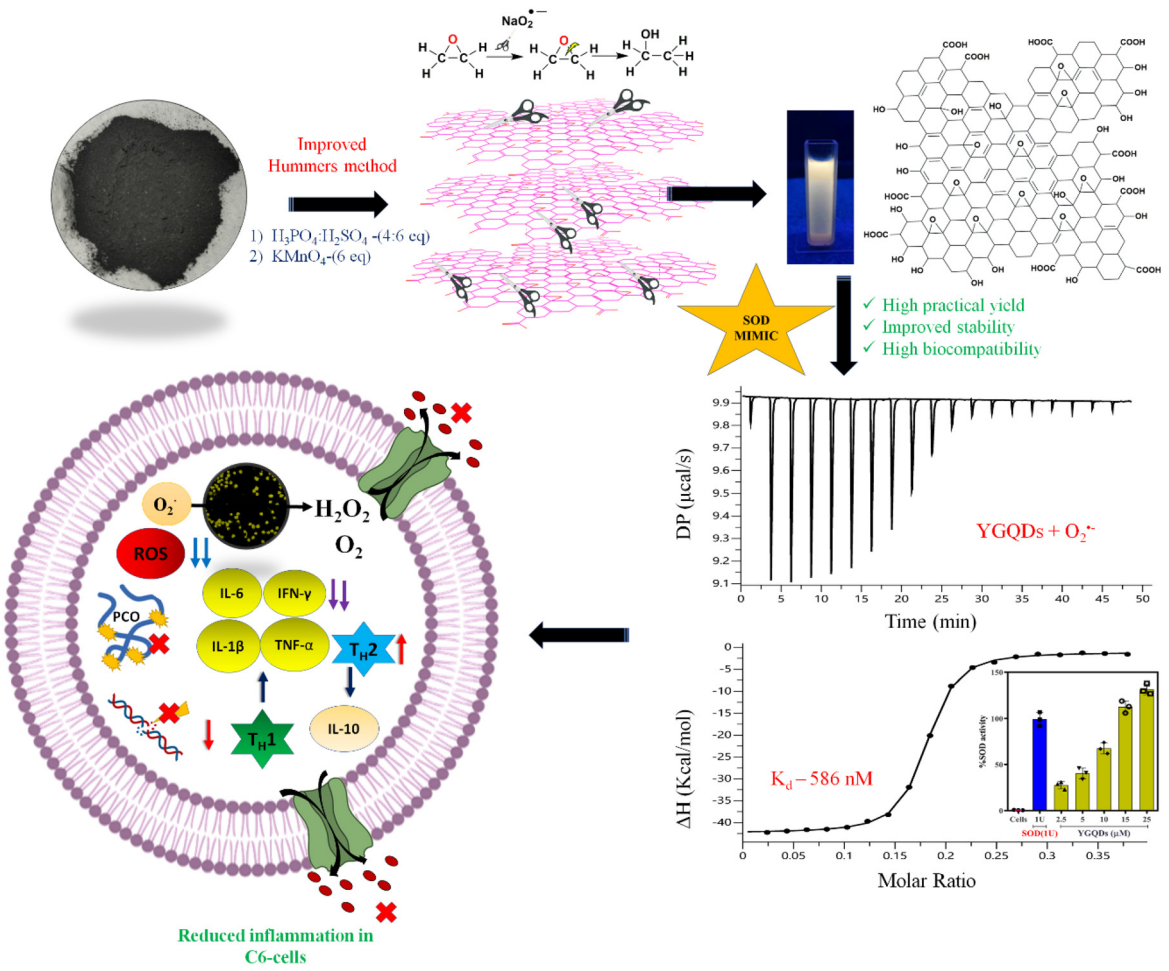

Scheme 1 Schematic illustrations of YGQDs synthesis, characterization, $O_2^{\bullet-}$ with K_d values, and antioxidant effect with selective SOD-like activity against oxidatively-stressed C6-cell survival indicating the roles of pro-inflammatory and anti-inflammatory cytokines release.

done using a dialysis bag of pore size 3000 Da for 12 h, wherein we noticed that all the YGQDs remained inside the dialysis bag, while the same upon dialysis through higher pore size bags ~5000 Da bag were completely lost. This indicates the possibility of YGQDs being in the size range of 3000–5000 Da. Furthermore, CHO elemental analysis supported with TOF-mass analysis was done to estimate the M.W. of YGQDs accurately. The details of the results of TOF-mass are shown in Fig. S2.† The elemental percentage of purified YGQDs shows 68.89% C, 4.82% H, and 24.87% O. The positive mode TOF-mass taken in the range 3–5 kDa shows molecular components at m/z = 2999.858, 3157.9063, 3576.7517, and 3708.513. Among the four, the highest molecular component is 3157.9063 $[M + Na]^+$ with calc. mass m/z = 3157.9177 and an empirical formula of $C_{184}H_{157}O_{48}Na^+$. Based on the findings, we speculate the appropriate mass of YGQDs to be 3157.94 Da. Besides, the determined structure of YGQDs also shows higher surface oxygenated surface groups and lower sp^2 centers. Next, we optimized the reaction condition by increasing the radical concentration, where we noticed that beyond the optimum range, trace levels of black precipitate were observed. The temperature optimization suggests that YGQDs formation occurs more efficiently at 121 °C, beyond which the formation of a black precipitate with diminished yellow and green fluorescence with practical yields > 50–60% are seen. This indicates that the degradation of the GO matrix occurs at high temperatures and due to unreacted radical induction. The results allowed us to select YGQDs for further study. The optimized conditions are summarized in Table S1.†

The FTIR spectrum, Fig. 1A, of GO shows absorption bands at 3335 cm^{-1} for stretching vibrations of O–H groups; the prominent bands appearing at ~1740 cm^{-1} and ~1628 cm^{-1} are ascribed to the stretching of C=O and C=C groups, respectively. The peaks at ~1223 cm^{-1} and ~1034 cm^{-1} are due to –C–OH and –C–O–C stretching and bending vibrations, respectively.[45] For YGQDs, the peaks at ~3335 cm^{-1} and ~1628 cm^{-1} represent the stretching vibrational patterns of OH and C=O groups, respectively. The sharp peaks at 1416 cm^{-1} indicate the in-plane vibrations of the carbon skeleton, which is common to graphitic materials. Finally, the low intense peaks at 1034 cm^{-1} are accounted for –C–OH stretching vibrations. The comparative spectral changes for both GO and YGQDs are shown in Fig. 1A. The X-ray photoelectron spectroscopy (XPS) patterns show the distribution of surface components in YGQDs with two signatures regions, C 1s and O 1s appearing at ~282 eV and ~584 eV, respectively (Fig. 1B). The deconvolution of O 1s spectrum shows three prominent peaks at 530.9 eV and 532 eV, representing the existence of C=O and C–OH groups, respectively. The low-order peaks at 535.2 eV represent C–O–C groups. The deconstruction of C 1s shows three major areas for C=C (sp^2), C–O (sp^3), and C=O groups, shown at 284.5 eV, 286.5 eV, and ~287.7 eV, respectively. The results of the deconvoluted regions of C 1s and O 1s shown in Fig. 1C and D were found to be as per earlier published reports.[48,49] The Raman spectra were used to illustrate the nature of defects. In GO, the peaks shown at 1329 cm^{-1} are assigned to the D bands, while the latter peak at 1585 cm^{-1} symbolizes G bands, a characteristic of graphene derivatives. Moreover, the minimal rise in the G band intensity compared to the D band represents greater sp^2 links in GO; the calculated I_D/I_G ~0.85 suggests a larger sp^2 domain and the presence of a multilayer.[50,51] In contrast, YGQDs showed highly intense D bands and low intense G bands appearing at ~1340 cm^{-1} and ~1552 cm^{-1} due to the changes in the oxidation levels. Moreover, the calc. I_D/I_G value of 0.91 suggests the high probability of defects and partial distortions in YGQDs.[52] The details of the Raman spectrum of GO and YGQDs are shown in Fig. 1D. Finally, the p-XRD patterns of GO showed peaks centered at (2θ ~10.18°, d = 0.8 nm), attributed to the (002) facet of GO.[53] In contrast, YGQDs peaks appeared at (23.8°, d = 0.316), attributed to the (002) graphitic facets, indicating the restoration of hindered networks (Fig. 1F). We also observed a typical larger d spacing corresponding to the existence of more surface oxygenated groups. Next, using the full width at half maximum (FWHM) of YGQDs diffraction peak and the Debye–Scherrer formula, the average crystalline size of YGQDs was estimated to be ~10 nm.[54,55]

The crystallinity and surface morphology of YGQDs observed through HR-TEM show the presence of a uniform distribution of circular dots at 100 nm (Fig. 2A), while the larger view of the dots can be seen at 50 nm magnified scale (Fig. 2B). Fig. 2C and D shows the presence of uniform circular shaped dots at 10 nm scale with the average size of YGQDs in the range of 7 ± 1.5 nm. Further, the magnified view of the dots in Fig. 2E shows a prominent lattice fringe with a d value of ~0.314 nm. The small deviation of the d value ~0.036 nm from ideal graphite is attributed to the abundance of oxygenated groups. Finally, the SAED taken under perpendicular electron beam projection showed a crystalline pattern in the basal plane of YGQDs (Fig. 2F). The EDS map taken for YGQDs shows a higher oxygen content of 11.52% and a lower carbon content of 88.74% when contrasted with that of GO, as shown in Fig. S3.†

Photophysical properties of YGQDs

Upon testing for solubility in polar and non-polar solvents, the YGQDs were found to be only soluble in water while they remained insoluble in other solvents (Fig. S4†). Such altered dispersibility in YGQDs arises from its intrinsic confinement effect and edge states that show altered interactions with solvent molecules. Furthermore, the YGQDs demonstrated stability with no aggregation observed after 6 months of long-term storage at room temperature. The UV-vis spectra of YGQDs recorded in Milli-Q water show two distinct absorption bands at ~235 nm and ~274 nm, representing the π–π* transition arising from sp^2 links and n–π* transitions arising from defects, respectively (Fig. 3A). The UV-vis spectra of synthesized GO from CW and its related explanation are shown in Fig. S5, ESI.† Next, pH-triggered fluorescence studies were performed to study the effect of pH on the photo-controlled stability of YGQDs. The results show shifting in the UV-vis spectra at different pH (Fig. S6A, ESI†). We also noticed significant shifting in the photo-luminescence (PL) spectra upon moving

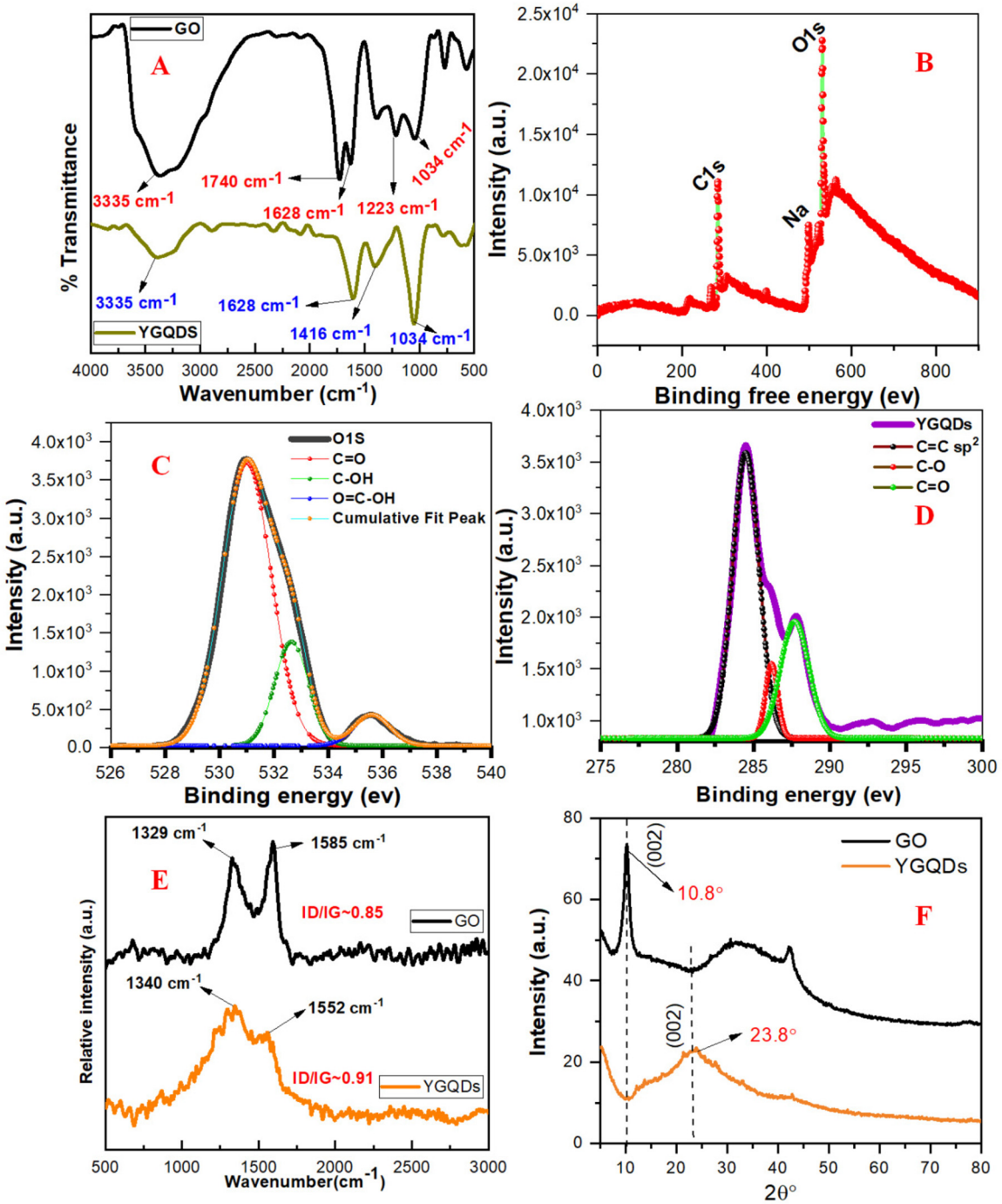

Fig. 1 (A) FTIR-ATR spectra of GO and YGQDs. (B) Overall XPS survey of YGQDs, with C 1s and O 1s levels. (C) O 1s levels showing O═C, C–O–C, and C–OH groups. (D) Deconvoluted C 1s core levels showing C═O, C–O–C, and C–OH groups. (E) Raman spectra of GO and YGQDs showing characteristic D and G bands. (F) Powder XRD pattern of GO and YGQDs.

from pH 3 to 10 along with the peak broadening effect beyond pH 8 due to the edge overlap and large domain size in YGQDs. Moreover, the protonation and de-protonation effect of the functional groups at different pH values shows a typical change in the rate of transition and the inherent property of YGQDs that results in the shifting of emission maxima to higher wavelengths, *i.e.*, giving rise to an excitation-independent phenomenon.[56] The results of the PL shifts occurring at different pH values are shown in Fig. S6B–F, ESI.† In addition, we noticed an acute emission peak with ε_{max} ~530 nm at pH 7, which arises due to radiative transitions, while the same under an acidic environment is nearly reduced to half. The formation of new peaks beyond 530 nm indicates plausible non-radiative intra-band shifts in YGQDs.

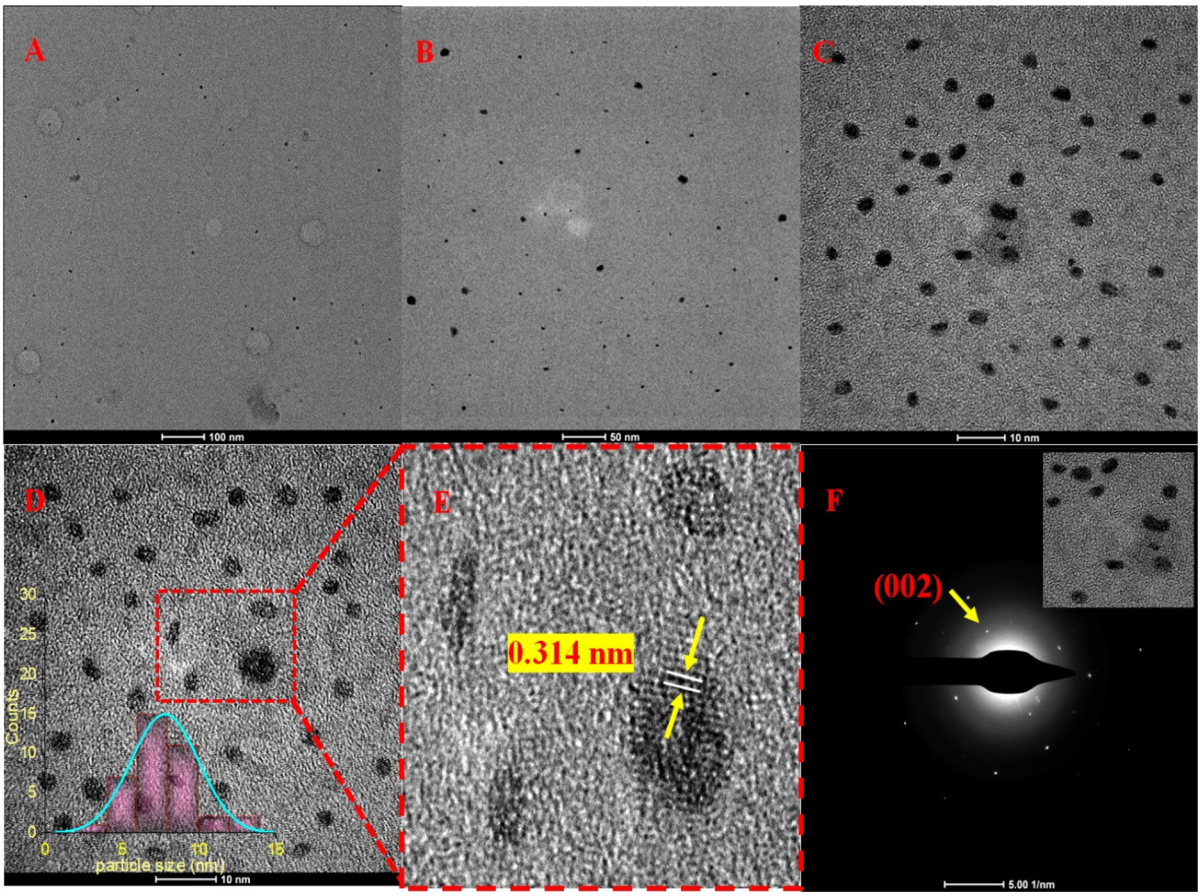

Fig. 2 Surface morphology of YGQDs captured by HR-TEM at (A) 100 nm, (B) 50 nm, (C) 10 nm, (D) 10 nm scale, (E) zoomed YGQDs and (F) SAED patterns of YGQDs.

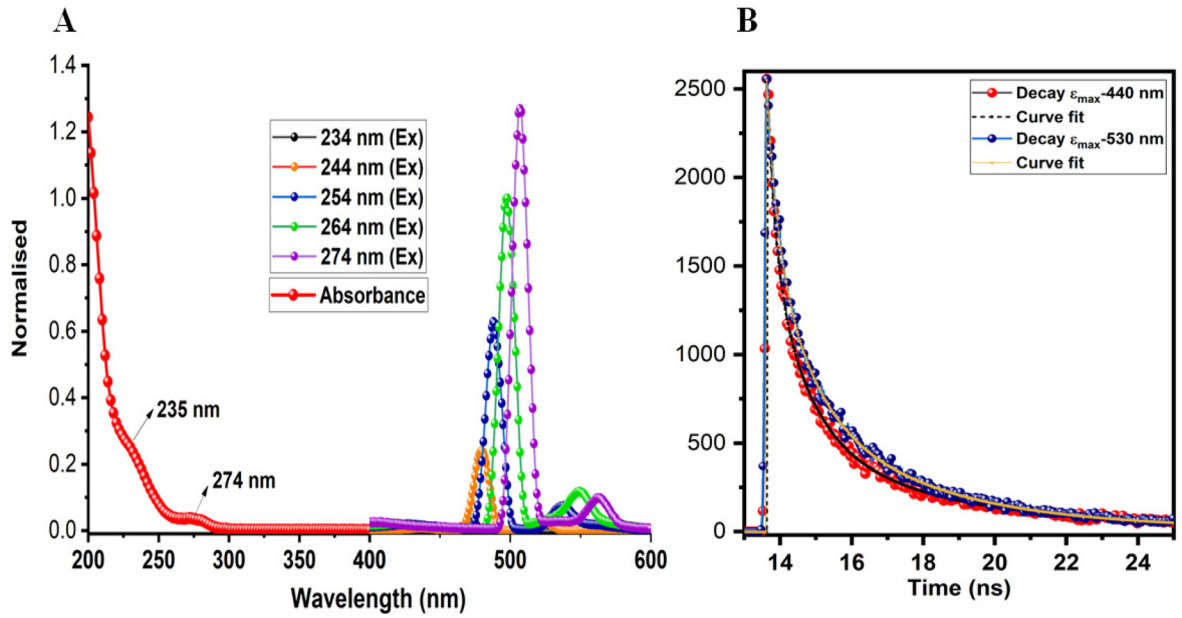

Fig. 3 (A) UV-Vis spectra of YGQDs (red) and PL spectra of YGQDs recorded at different excitation wavelengths (234 nm → 274 nm). (B) Picture representing the ns lifetime decay of YGQDs at 440 nm (red) and 530 nm (blue), respectively.

Next, time-resolved fluorescence (TRF) measurements were carried out to quantify the role of carriers in maintaining photo-dynamics. The results are summarized in Table S2.† The tri-exponential curve fitting along with the fluorescence decay shows that relaxation occurs, *viz.*, three different pathways (eqn (i)[57]), with B_1, B_2, and B_3, indicating the amplitudes of a lifetime. τ_1 signifies the intrinsic aromatic sp^2 domains, and τ_2 and τ_3 indicate the lifetime due to the irrelevant surface groups. The higher value for τ_2 and B_2 indicates emission to be controlled by edge/basal states contributing toward a longer lifetime. The lifetime decay curve of YGQDs is shown in Fig. 3B. The calculated average lifetime for YGQDs was found to be 0.7 ± 0.26 ns and 1.17 ± 0.29 ns for (ε_{max} ~440 nm and ε_{max} ~530 nm, respectively) with χ^2 deviations of 1.06 and 1.11, respectively. The ns lifetime in YGQDs indicates the singlet nature of emission, with the luminescence dominated by surface defects.

$$\text{fit} = A + B_1 \times \exp\left(-\frac{i}{\tau_1}\right) + B_2 \times \exp\left(-\frac{i}{\tau_2}\right) + B_3 \times \exp\left(-\frac{i}{\tau_3}\right). \quad \text{(i)}$$

Radical scavenging activity (RSA) and biocompatibility studies of YGQDs

We have seen earlier that nanozymes' catalytic performance primarily depends on their structural properties like size, morphology, functional groups, and presence of defects.[58–60] Unlike other classes of inorganic nanoparticles and carbon quantum dots (CDs), GQDs offer high C=C conjugation and charge transfer mobility with additional surface-oriented structural defects that allow them to act as hydrogen bond donors and radical stabilizers to quench free radicals.[61] Hence, to investigate the RSA and its associated enzymatic roles, we first analyzed the antioxidant properties of YGQDs *in vitro* using the DPPH radical assay. Under optimal conditions, DPPH represents a stable free radical (DPPH°) that shows a characteristic λ_{max} at 517 nm. The decrease in the absorbance of DPPH° due to the formation of stable DPPHH estimates the RSA. The RSA of YGQDs (0–100 μM) was measured and compared to standard AA. We noticed a prominent RSA in YGQDs in a dose-dependent order and with higher efficiency than AA (Fig. 4A). The calculated EC_{50} was found to be ~12 μM for YGQDs and ~55 μM for AA, *i.e.*, a net 4.5-fold better activity for YGQDs. The colorimetric changes for RSA estimation by the DPPH assay are shown in Fig. 4B. The high RSA activity of YGQDs accounted for more hydrogen donor and sp^2 center participation toward radial stabilization by forming a stable crystal plane. These preliminary results of the DPPH assay further encouraged us to evaluate the anti-oxidative role of these YGQDs in different cellular models under the influence of OS.

The biocompatibility of YGQDs was next evaluated before their antioxidative examination in *ex vivo* models to determine its safety. The cytotoxicity measurements of YGQDs were performed using PBMCs. The results of the cytotoxicity studies are shown in Fig. 4C. We noticed almost insignificant toxicity at high treatment doses of YGQDs, *i.e.*, with 500 μM treatment, showing <15% PBMC killing. Contrastingly, AmB taken as a positive drug standard showed ~65% killing at only 100 μM. In addition, we also noticed very minimal hemolysis in YGQDs, with only 12% hemolysis ($P < 0.001$) at 500 μM (Fig. 4D). While AmB, which was used as a positive control, showed 100% hemolysis at only 100 μM, indicating high hemolytic activity and toxicity than YGQDs.[62] The pictures of the hemolytic effect of YGQDs and AmB at different concentrations with human blood samples are shown in Fig. S7.† The low cytotoxicity and hemolysis effect revealed that the biocompatibility range of YGQDs was very high. Furthermore, considering its safety, the tested doses of YGQDs in *ex vivo* assays were taken 4-fold less than the determined toxicity doses.

Ex vivo antioxidant role of YGQDs

Encouraged by the excellent biocompatibility of YGQDs, the step-wise assessment of cell survival ability and RSA of YGQDs in the *ex vivo* setup were studied as per the earlier established procedure.[63] We selected three different cell lines based on their susceptibility toward reactive radical species. The related survivability and RSA were measured using the MTT assay. Primarily, all three cell lines, namely, C6-cells (neural cells), HepG2 (human liver cancer cell line), and Caco-2 (human colorectal adenocarcinoma cells), were inducted with 200 μM H_2O_2 to induce severe ROS. Next, the ability of YGQDs to rescue cells from ROS was monitored in both the presence and absence of YGQDs at different concentrations (2.5–25 μM). Interestingly, we noticed that the cell survival decreased below 10% upon H_2O_2 induction, whereas the same upon YGQDs treatment showed a systemic increase in survival. The survival rates were estimated as ~90%, ~80%, and ~75% for C6-cells, HepG2 cells, and Caco-2 cells, respectively, at only 25 μM treated dose (Fig. S8A–C†). Interestingly, amongst all the tested cells, we noticed that the ability of YGQDs to alleviate ROS in C6-cells was more prominent than AA with EC_{50} ~25 μM YGQDs and beyond 100 μM for AA (Fig. 4E). The results imply that the YGQDs, irrespective of the nature of cells, can be well internalized and can protect the C6-cells majorly from severe OS-mediated cell death. Based on this high RSA response of YGQDs toward C6-cells, next, we used lipopolysaccharide (LPS)-induced neuro-inflammation and ROS against C6-cells as a model system to evaluate the efficacy of YGQDs. We noticed that the YGQDs were able to scavage intracellularly generated ROS in a dose-dependent manner, measured using H_2DCFDA-based fluorescence in LPS-treated C6-cells (Fig. 4F). The results further confirmed the extent of cell survival is an intrinsic function of YGQDs. In the presence of 0.35 μM LPS, cell survival decreased to ~21% from 100%. However, the same with YGQDs pre-treatment showed increased survival of ~65%, ~78%, ~87%, and 96% for concentrations of 2.5, 5, 10, and 25 μM, respectively. The color change in the MTT plates showing C6-cell survival upon the incubation of YGQDs is illustrated in Fig. S9, ESI.†

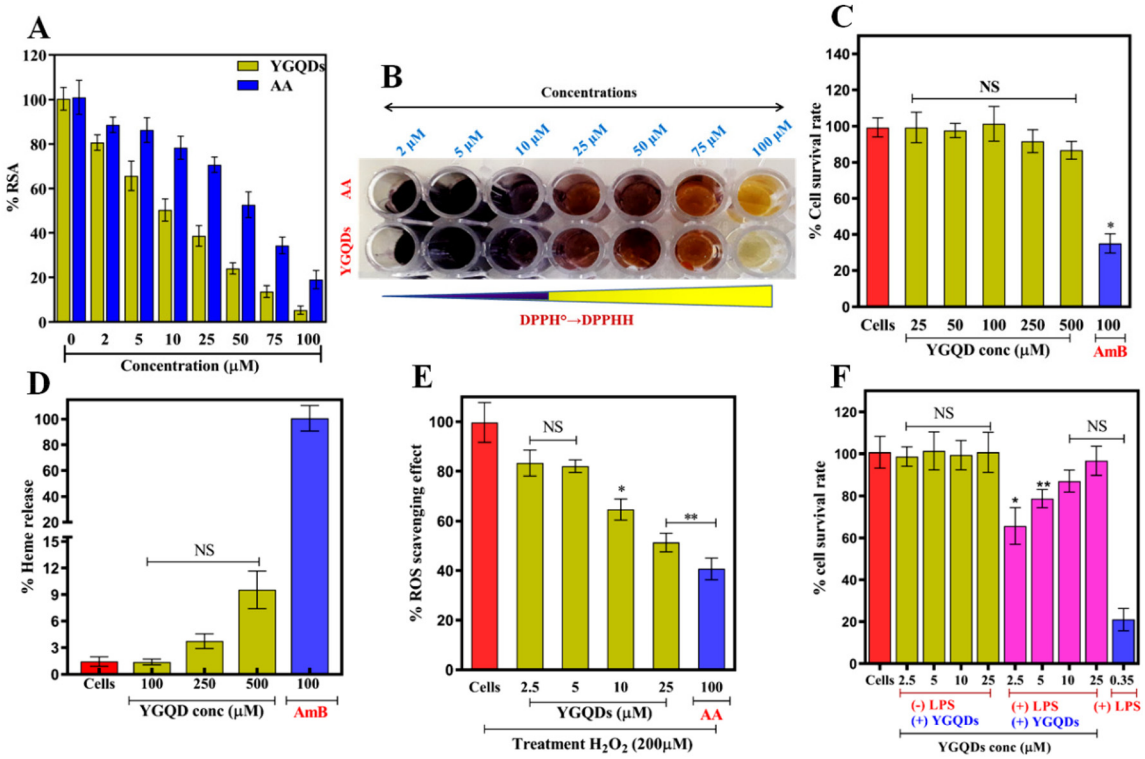

Fig. 4 (A) DPPH radical reduction showing percentage radical inhibition for YGQDs and AA, (B) color change due to the conversion of DPPH° to stable DPPHH, with decreasing purple color. Graphs representing (C) cytotoxicity of YGQDs against PBMC, (D) heme release with RBC with AmB as a positive control, (E) H_2DCFDA dye-based ROS evaluation with H_2O_2-treated C6-cells in the presence and absence of YGQDs and AA, and (F) MTT assay-based cell survival LPS-treated C6-cells in the presence of YGQDs.

Nanozyme activity in YGQDs

Following *in vitro* and *ex vivo* antioxidative property determination in YGQDs, its associated enzymatic activity was investigated for plausible SOD, GPx, and CAT-like activity due to their active role in balancing the cellular integrity by countering free radical-induced damage. Amongst the various peroxidases seen so far, GPx abundance is very high in mammalian systems due to its catalytic preferences toward oxidized lipid peroxides. Yet another class of enzyme in the biological system that is even more important is SOD due to its catalytic role in converting the primary generated $O_2^{\bullet-}$ to less toxic H_2O_2 within the cellular system. Further, the H_2O_2 produced in the later steps is degraded to H_2O (by GPx) and $H_2O + O_2$ (by CAT). So far, much attention is paid to carbon-based nanozymes with either explicit or implicit natural or induced peroxidase and/or CAT-like acitivity.[64] However, progress using GQDs for the same purpose is still in its infancy. Although it can be presumed that the carbon quantum dots (CDs) and GQDs share similar surface architecture and functional group composition, the latter can behave more like an enzyme active site. The circular structure observed through HR-TEM shows a dispersed, narrower size distribution of YGQDs with avg. size ~7.5 nm. The small size of the nanocrystallites increases the specific surface area and the presence of more functional groups on the crystal surface. More oxygenated functional groups in the peripheral location show more trapping of $O_2^{\bullet-}$.[65,66] Furthermore, theoretically predicted models suggest that the presence of functional groups like COOH and OH can act as the substrate-binding sites.[25] Using the above interpretation, we next tested the GPx and CAT activities of YGQDs using 3,3′,5,5′-tetramethylbenzidine (TMB) as a chromogenic probe and H_2O_2 as a radical initiator. The results of the GPx and CAT effect of YGQDs at different concentrations and its comparison to natural Horseradish peroxidases (HRP) and CAT enzymes are shown in Fig. S10A and B, ESI.† The results show very minimal GPx activity when tested at different concentration of YGQDs. However, HRP(1U), taken as a positive control, showed significant changes in the GPx activity. Similarly, the extent of H_2O_2 degradation, measured by calculating the reduced absorbance at 240 nm, showed trace CAT activity in YGQDs when compared to natural CAT. With no associated GPx or CAT-like activity, the YGQDs were next screened for plausible SOD-like activity. The results of the SOD activity of YGQDs are shown in Fig. 5A. Surprisingly, we found robust SOD-like activity in YGQDs wherein 15 μM YGQDs equaled the activity of 1U bSOD enzyme. Such high specific SOD-like activity can be related to the generation of more sp^3 and lesser sp^2 regions in the carbon skeleton resulting from the oxidative conversion of GO to YGQDs. Additionally, the increased specific surface area of

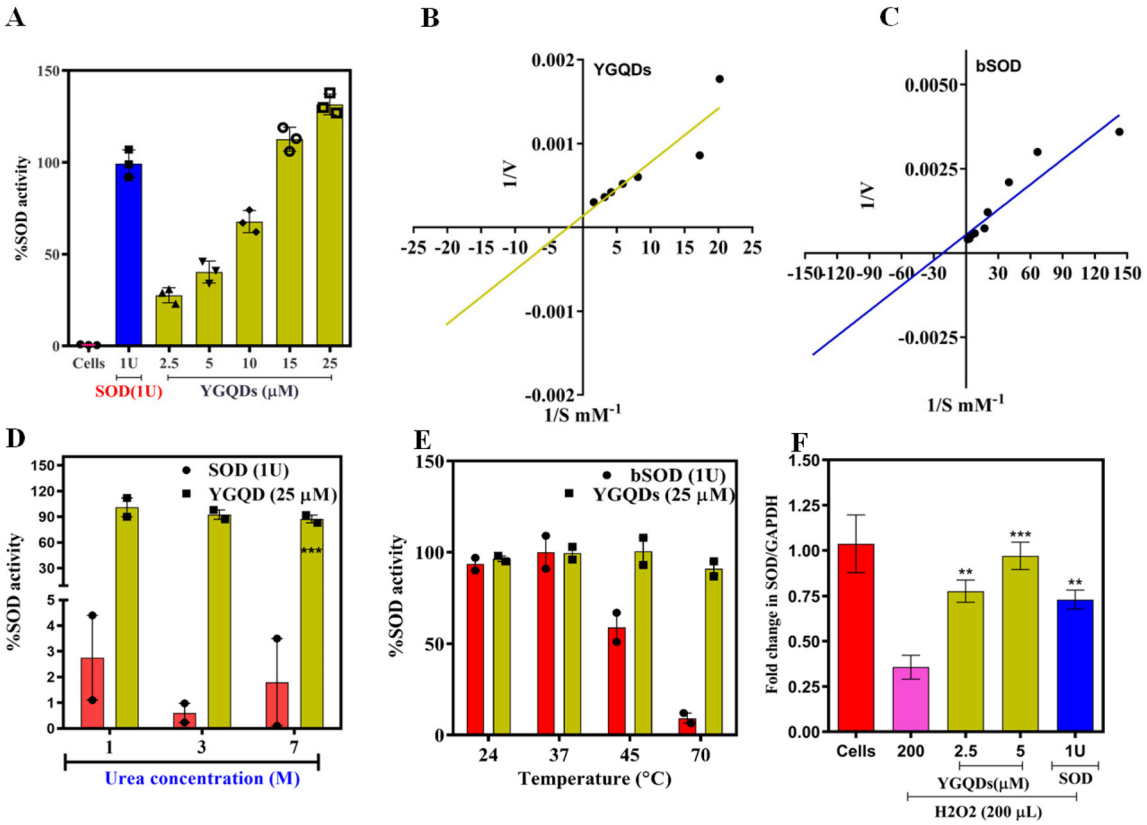

Fig. 5 (A) SOD-like enzyme activity of YGQDs (2.5–25 μM) *vs.* bSOD (1U). Calculation of K_m and V_{max} from Lineweaver Burk (L–B) plot of (B) bSOD and (C) YGQDs for the determination of K_m and V_{max}. Stability studies of YGQDs at (D) different temperatures (E) and with varying concentrations of denaturant (urea). (F) Changes in gene expression levels after YGQ and bSOD pre-treatment following ROS generation.

the circular dots (earlier discussed) due to fragmentation allows them to act as catalytic sites to mediate the enzymatic reaction. These structural defects initiate the formation of hydrogen bonds and static interactions to counter the $O_2^{\bullet-}$ while the lesser sp^2 crystal plane operates through Π-bonded interactions to stabilize these radicals.

The kinetic studies of SOD activity of YGQDs

We performed SOD enzyme assay using pyrogallol as the substrate and determined the kinetic parameters like V_{max} and K_m through Michalis–Menten (M–M) kinetics. The decreased absorbance of pyrogallol (at 325 nm) due to its auto-oxidation in the presence of the generated $O_2^{\bullet-}$ radical is a well-established model to study the SOD-like activity; hence, it was used. We noticed the SOD activity of YGQDs to be highly selective and the highest determined so far amongst all other graphene-based nanozymes.[28] The findings encouraged us further to calculate the kinetic parameters [Michaelis constant (K_m) and maximum reaction velocity, (V_{max})] using Michaelis–Menten (M–M) and Lineweaver Burk (LB) equations for both bSOD and YGQDs tested at different concentrations. The results indicate ~10-fold higher K_m but with a 10-fold lower catalytic turnover (K_{cat}) for YGQDs than bSOD (Fig. 5B, C and Table 1). While having a lower K_{cat} value for YGQDs than bSOD, almost comparable V_{max} can be obtained using a higher amount of YGQDs in the assay. Moreover, upon testing for the enzymatic performance in denaturants [urea (1–7 M)], we noticed the complete retention of SOD activity for YGQDs at urea doses as high as 7 M, while bSOD's activity drastically decreased below 5% under the same tested condition. The details of the effect of denaturants on the dismutase activity of YGQDs are shown in (Fig. 5D). We also studied the effect of temperature on the enzymatic performance of YGQDs. We noticed almost 99.8% and 100% SOD activity for YGQDs and bSOD, respectively, at 24 °C. Interestingly, at higher temperatures (beyond 45 °C and 70 °C), we noticed only 42.8% and 1.5% of SOD activity for bSOD whereas almost~ 85% and ~93% of activity retention was shown by YGQDs. This can be reasoned from the high thermal and colloidal stability of YGQDs arising from the

Table 1 Tabulation of the calculated kinetic parameters: K_m, V_{max}, and K_{cat} for both SOD and YGQDs from LB plots

Kinetic parameters obtained from M–M kinetics				
	V_{max} (μmol S^{-1})	K_m (μM)	K_{cat} (S^{-1})	K_{cat}/K_m (S^{-1})
bSOD	1943	40	777	1.9×10^7
YGQDs	1358	420	77.6	1.8×10^5

inertness of the carbon skeleton. The results indicate that YGQDs as nanozymes are stable and can maintain their activity under harsh conditions. Additionally, the antioxidant and SOD activities associated with it suggest that possibly the highly oxidized groups in YGQDs make carbon domains electro-deficient, allowing them to act as shuttles to counter $O_2^{\bullet-}$ alongwith its circular structure that helps them entrap more radicals.[67] Perhaps it is seen that in the presence of denaturing agents and at temperatures beyond 30 °C, an irreversible reduction of the biological activity of enzymes happens due to the loss of its 3D protein folding. However, such limitations do not apply to YGQDs.

Gene expression studies after YGQDs treatment

Following nanozyme activity measurement, SOD, CAT, and GPx gene expression profiles were measured from the isolated RNA and cDNA from bSOD- and YGQDs-treated C6-cells.[44] We noticed that the treatment of C6-cells with H_2O_2 resulted in a reduction of the expression levels of genes for the enzymes SOD, CAT, and GPx. After pre-incubation with YGQDs, we observed a dose-dependent recovery in the expression of these genes. Here, the change in the expression of the housekeeping gene glyceraldehyde-3-phosphate dehydrogenases (GAPDH), whose expression remains unaltered, is used as a control. Almost ~3-fold and ~2.1-fold recovery of the SOD gene expression was obtained after pre-incubation with 5 μM and 2.5 μM YGQDs, respectively (Fig. 5F). The CAT and GPx gene recovery showed a net ~1.5-fold change with 5 μM YGQD, as shown in Fig. S11A and B.† Therefore, the gene expression studies correlate well with the SOD activity of YGQDs since a more significant change in gene expression is achieved for bSOD, indicating that the target of YGQDs is SOD and not CAT or GPX.

Binding affinity of YGQDs and bSOD toward $O_2^{\bullet-}$

To confirm the high specific binding of $O_2^{\bullet-}$ onto the surface of YGQDs, Isothermal Calorimetry (ITC)-based measurements were done. The thermodynamically-derived parameters are outlined for both YGQDs and bSOD. The details of the ITC-method are illustrated in the ESI.† We took pyrogallol as our model substrate due to its ability to generate $O_2^{\bullet-}$ under milder conditions, high water-solubility, and catalyst-free autoxidation under an alkaline buffer (pH ~8, Tris-EDTA). The shift of the UV-vis spectrum due to auto-oxidation shows a synchronous increase in the peak at 320 nm, resembling the conversion of pyrogallol to semi-quinone radical and $O_2^{\bullet-}$. The binding affinity of the formed $O_2^{\bullet-}$ with YGQDs and bSOD were compared. So far, as such, there are no reports wherein direct ITC-based measurements have been employed to estimate the binding kinetics associated with $O_2^{\bullet-}$quenching using the bSOD enzyme even though its crystal structure has indicated specific interacting residues of bSOD responsible for the binding of $O_2^{\bullet-}$. The results depict a strong negative enthalpy change (ΔH) determined from the amplitude, indicating an exothermic process. The obtained K_d values from the plot of (ΔH *vs.* Molar ratio) show 586 nM for YGQDs and 57.3 nM for bSOD (Fig. 6A and B). Even though the YGQDs exhibit slightly lower K_d than bSOD for $O_2^{\bullet-}$, the binding isotherms follow a similar thermodynamic pattern, representing a highly favorable exothermic reaction. Moreover, having almost similar negative Gibbs free energy (ΔG) for YGQDs and bSOD, it can be considered that the binding of $O_2^{\bullet-}$ to YGQDs or bSOD is spontaneous and endergonic. The determined parameters from the ITC analysis are shown in Table 2. More importantly, we noticed no binding or saturation isotherm when there was no generation of $O_2^{\bullet-}$ (like in alkaline buffer, *i.e.*, Tris + EDTA or in the presence of pyrogallol alone). These results suggest that the binding isotherm is a function of generated $O_2^{\bullet-}$ only (Fig. 6C and D). Besides, the high ΔH and ΔS values calculated for YGQDs indicate a multidomain capture of $O_2^{\bullet-}$ on the YGQDs surface.

Anti-apoptotic activity of YGQDs against H_2O_2-induced C6-cell apoptosis

To access the anti-apoptotic roles of YGQDs, H_2O_2-induced cell apoptosis and death were estimated both in the presence and absence of YGQDs using flow cytometry under *ex vivo* conditions. The results of the flow cytometry are illustrated in Fig. 7A. As expected, the YGQDs were able to inhibit C6-cell apoptosis in a dose-dependent fashion. Thus, upon treatment with 200 μM H_2O_2 for 6 h, more than ~31% cell apoptosis was noticed, determined by the increase in Annexin V-FITC-stained C6-cells. Upon treatment with YGQDs, the same cells showed a gradual decrease in apoptotic cells of ~23.9%, ~11%, and 5.3% for the tested concentrations of 2.5, 5, and 10 μM YGQDs, respectively. Furthermore, with bSOD as a positive control, the apoptotic reduction was only ~8.1%. Moreover, the study did not reveal any C6-cell necrosis with YGQDs treatment, measured from the number of propidium-iodide (PI) stained cells. Together, the results indicate that OS-mediated apoptosis caused by H_2O_2 can be well suppressed upon treatment with YGQDs and its strong RSA and cytoprotective activity.

Next, the lipid peroxidation (LPO) products generated through membrane lipid oxidation and protein carbonylation (PCO) constitute the main markers for measuring OS-mediated cell damage. We presumed that the strong anti-oxidative behavior of YGQDs can also decrease the elevated levels of LPO and PCO under the influence of OS. The assay was conducted considering the conversion of generated LPO to malondialdehyde (MDA), which when reacted with thiobarbituric acid (TBA), produces a colorimetric change with an increased absorbance (λ_{max}) at 532 nm. The MDA and PCO levels estimation findings are shown in Fig. 7B and C. The results show a net ~3.4-fold increase in the LPO level with 200 μM H_2O_2 treatment for C6-cells (Fig. 7B). In the presence of 25 μM YGQDs, the LPO levels were reversed to normal. The change in the color intensity during MDA-TBA conversions was studied using ELISA and is shown in Fig. S12, ESI.† In a parallel study, we observed that the PCO was increased to ~4.3 fold after 200 μM H_2O_2 treatment but was eventually reversed to normal with only a 25 μM treatment dose of YGQDs. The net reduction in LPO and PCO levels with increasing doses indicates that YGQDs can protect C6-cells from OS injury by acting as a strong radical quencher.

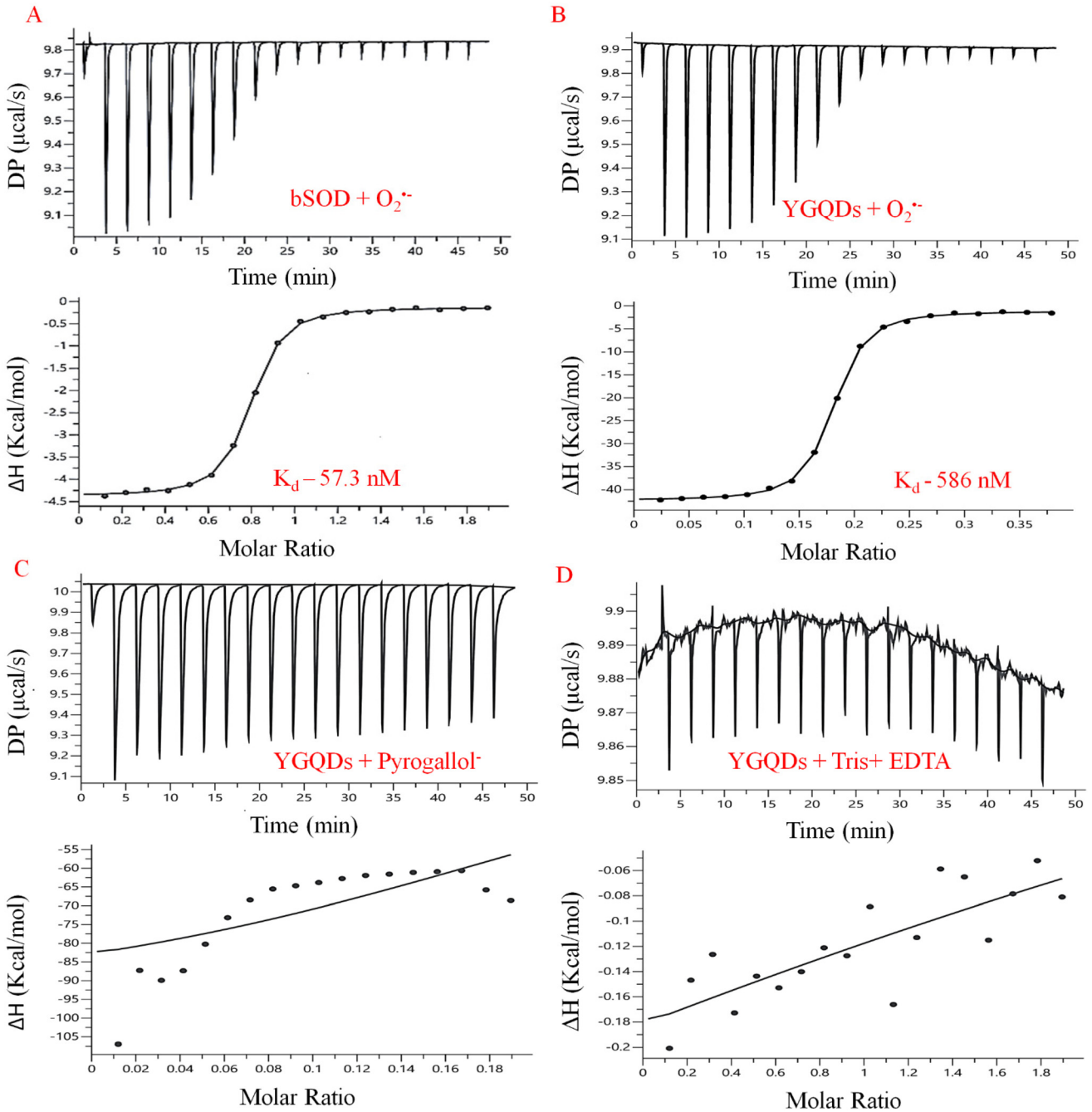

Fig. 6 Determination of YGQD and bSOD binding towards superoxide ion by isothermal calorimetry, ITC with (A) bSOD in the presence of pyrogallol + alkaline buffer, (B) YGQDs in the presence of pyrogallol + alkaline buffer, (C) YGQDs in the presence of pyrogallol only, and (D) YGQDs in the presence of Tris-EDTA alkaline buffer only.

Table 2 The calculated values of different thermodynamic parameters for both bSOD and YGQDs determined using the ITC method

	K_d [a]	ΔG^a	ΔH^a	$-T\Delta S^a$
SOD	57.3 nM	−8.5	−4.13	−4.37
YGQD	586 nM	−9.88	−41.2	−7.91

[a] K_d: dissociation constant; ΔG: Gibbs free energy; ΔH change in enthalpy, T temperature in Kelvin scale, and ΔS: entropy change.

YGQD inhibits the production of pro-inflammatory cytokines

Often, it is seen that prolonged OS in C6-cell and other related cells results in a severe imbalance between released pro-inflammatory and anti-inflammatory cytokines, which causes cellular inflammation, followed by cell/DNA and tissue destruction.[68,69] Hence, we explored the possibility of YGQDs controlling the cytokine release pattern under an *ex vivo* cellular setup. Based on our initial findings, YGQDs are critical in

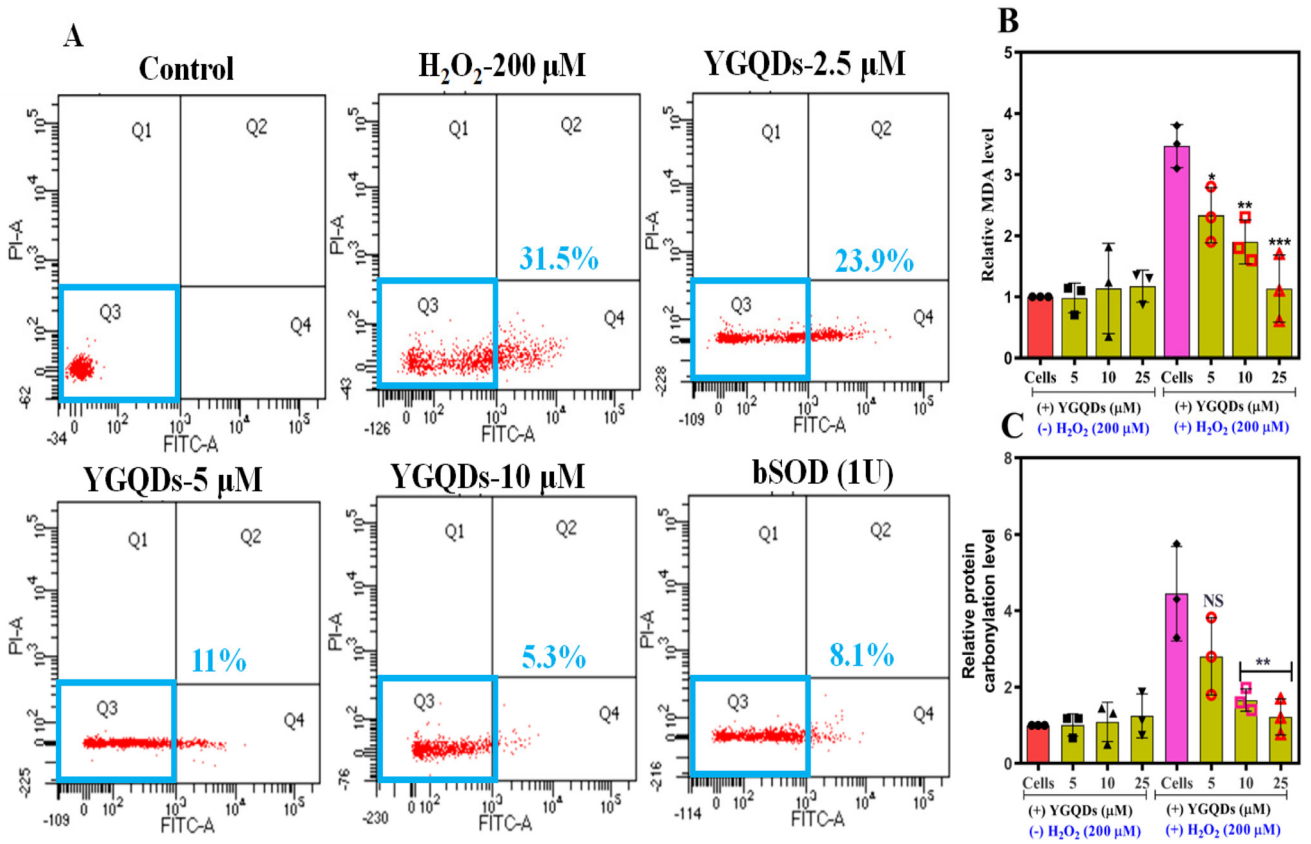

Fig. 7 (A) FACS analysis of H_2O_2-treated C6-cells with or without the pretreatment of YGQDs (2.5–10 μM) and bSOD (1U) after staining with Annexin-V-FITC and propidium iodide. (B) Lipid peroxidation assay with YGQDs (5–25 μM). (C) Protein carbonylation assay with YGQDs (5–25 μM).

balancing OS and show the highest cell protection toward C6-cells. Next, we used ELISA to measure its controlling effect in maintaining the altered levels of various pro-inflammatory (IFN-γ, TNF-α, IL-6, and IL-1β) and anti-inflammatory (IL-10) cytokines under OS. The result of the multiple cytokines release pattern before and after the induction of YGQDs and bSODs is shown in Fig. 8A–E. We found that the expression of pro-inflammatory cytokines IFN-γ, TNF-α, IL-6, and IL-1β increased to ~4.6, ~3.5, ~3.2, and ~2.1 fold upon 200 μM treatment of H_2O_2. These sudden increases in the pro-inflammatory cytokines are physiologically significant determinants of neurodegenerative disease and other associated diseases. Interestingly, upon treatment with C6-cells with only lower concentration of YGQDs (*i.e.*, 2.5 and 5 μM), the expression level of all pro-inflammatory cytokines was significantly reversed to the basal level. The results obtained for YGQDs were comparable to 1 μM bSOD (Fig. 8A–D). Inversely, we displayed the expression of the anti-inflammatory cytokine IL-10, which is highly decreased with H_2O_2-treatment (by ~3 fold), were elevated back to its basal level in the presence of YGQDs (Fig. 8E). Considered together, these data of expression levels of different cytokines during cellular OS suggest that the imbalance of pro- and anti-inflammatory cytokines, which are created due to the OS in *ex vivo* models, are restored to normal with only 5 μM treatment of YGQDs. Interestingly, earlier, during *in vitro* SOD activity assessment, we noticed that 15 μM treatment dose of YGQDs equaled the activity of 1U bSOD. However, during the *ex vivo* studies using ELISA, we observed that only 5 μM YGQDs was equivalent to 1 μM bSOD, indicating its better activity upon cellular intake. Earlier, Guo *et al.* showed a similar study using $MoSe_4$ NPs intended for colitis treatment, but the activity observed was much lower than our YGQDs.[70] These findings forecast that YGQD has the potential to be implemented as a therapeutic candidate inside the cell for the treatment of neurological disorders and possibly other diseases that originate due to OS.

Cellular localization and cytoprotective activity of YGQDs

The cellular uptake of YGQDs inside C6-cells and its related effect upon internalization were determined using confocal fluorescence microscopy. The results of the time-dependent cellular uptake of YGQDs are shown in Fig. 8F. The YGQDs, due to their intrinsic excellent yellow fluorescence, were used directly without any secondary labels. We noticed that at time t = 0 min, no fluorescence was observed; however, following 1 h and 3 h of treatment with C6-cells, we noticed the complete internalization of YGQDs with almost no change in the fluorescence intensity after 1 h and 3 h (Fig. 8F). The confocal measurements were done within a short exposure time to avoid cellular auto-fluorescence that can interfere with the

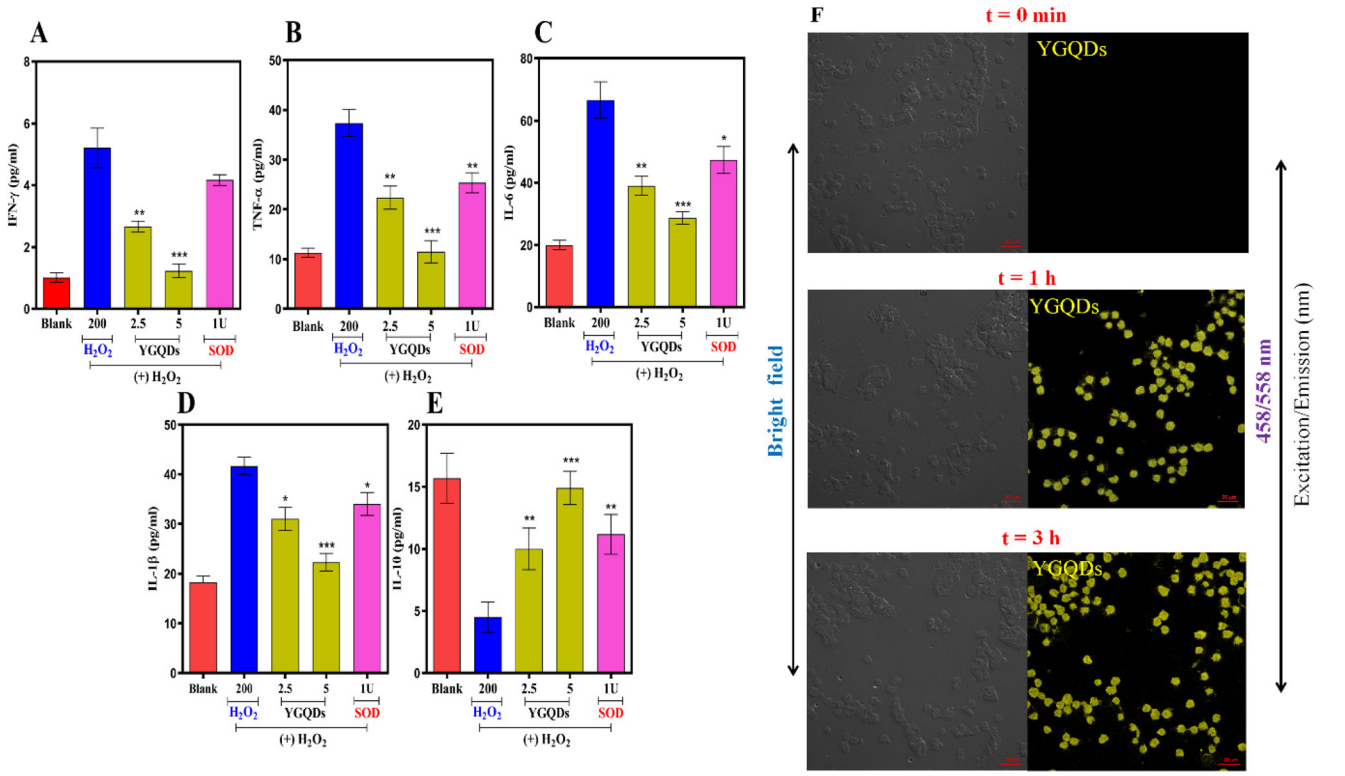

Fig. 8 Cytokine release pattern in the presence and absence of YGQDs and bSOD in H_2O_2-treated C6-cells (A) IFN-γ, (B) TNF-α, (C) IL-6, (D) IL-1B, and (E) IL-1β levels. (F) The image representing the cellular uptake of YGQDs (2.5 μM) by C6-cells was visualized under a confocal microscope at *t* = 0 min, 1 h, and 3 h, respectively.

original fluorescence of YGQDs. In addition, the untreated C6-cells taken as a control showed no fluorescence at any tested time points. This altered sub-cellular distribution of YGQDs can be reasoned from its caveolin-mediated endocytosis of YGQDs. We noticed the bright fluorescence of YGQDs within 1 h of treatment, indicating that the YGQDs were well internalized without damaging the membrane integrity. This can be correlated to its high biocompatibility. Further, the bright fluorescence in the C6-cell interiors suggests its plausible cytosolic localization. The internalization is greatly influenced by the hydrophilic and lipophilic functional groups that allow its permeation. Furthermore, the morphological changes studied using a phase contrast microscope show the resuscitation of ROS-mediated C6-cell damage in the presence of YGQDs (Fig. S13, ESI†). From the internalization studies, we further correlate that the synthesized YGQDs have shown highly biocompatible and increased cell survivability of ROS-inflated C6-cells under *ex vivo* conditions.

Discussion

OS presented by $O_2^{\bullet-}$ directly correlates with the pathophysiology of many diseases, including the progression of neurodegenerative diseases like Alzheimer's disease (AD) that are extensively triggered due to the loss of functions of natural enzymes like SOD, CAT, and GPx.[71,72] For example, familial amyotrophic lateral sclerosis (FALS) occurs due to the selective loss of motor neuron activity due to Cu, Zn-SOD gene modification.[73] In most cases, it is perceived that the over-expression or supplementation of recombinant SOD (rSOD) levels can prevent such ubiquitous generation of superoxides.[74,75] However, the major problem with rSOD is its poor cytoplasmic and nuclear distribution due to its low operational stability, high immunogenicity, low cellular uptake, lesser circulation half-lives, and poor shelf life. So far, only a few SOD-based conjugates have been synthesized that exhibit longer circulation half-lives, high stability, and lesser immunogenicity (polyethylene-liposome conjugated SODs).[76] However, using such polymer-liposome-based SOD mimics provides a high production/formulation cost and low clinical success rates. Hence, looking for a synthetic alternative with high stability and increased circulation half-life is still an unfulfilled goal. Carbon-based mimics are mainly used as adsorbents, photo-induced ROS generating agents, and co-delivery vehicles for PDT-based antimicrobial agents apart from some of their multifunctional nano-enzymatic properties, with their enzyme-specific activity still lacking behind.[77–79]

Considering the above challenges, we selected CW as our starting point to subsidize the fabrication cost of synthesizing specific nanozymes. The presence of highly stacked aliphatic domains and different functional groups allows its quicker fragmentation into nanozyme. Moreover, recycling waste materials into meaningful healthcare alternatives is a remark-

able commercialization strategy. GQDs are well established for their applications involving biosensors, drug-delivery formulations, bioimaging, *etc.*, due to their excellent structure-related activity and high biocompatibility. However, its use for the treatment of neurodegenerative diseases is very rare.[80] Herein, we have shown a simple strategy to synthesize YGQDs from CW. The obtained YGQDs were well characterized and exhibited an avg. size ~7 nm and M.W. 3197.90 Da. The fabrication mechanism depicted that the *in situ* formed $NaO_2^{\bullet-}$ acted like "molecular scissors" to cleave across C–O–C linkages of GO to produce circular YGQDs. Further, having shown excellent defect-driven PL, these YGQDs, when tested for *in vitro* screening anti-oxidative activity, showed prominent RSA that were later analyzed to be linked with high specific SOD activity. Further, upon transcribing to *ex vivo* conditions, the YGQDs showed high RSA for C6-cells and excellent biocompatibility. These findings allowed us to select C6-cells as our model substrate to explore the further antioxidative-associated role of YGQDs. The stability studies showed YGQDs to be highly stable over a wide range of temperatures (24–70 °C) and denaturants (*e.g.*, 7 M urea), unlike bSOD. Moreover, the strong binding interaction of $O_2^{\bullet-}$ radical for YGQDs estimated for the first time using ITC shows K_d in the nM range. Quite intriguingly, the binding affinity of YGQDs for $O_2^{\bullet-}$ shows a thermodynamically favorable spontaneous process with negative ΔG. With no crystal data available to quantify the binding interaction of CDs, QDs, and GQDs with $O_2^{\bullet-}$, the only published results from Gao *et al.* suggest that hydroxyl and carboxyl groups, like the case of our YGQDs, are the main contributors that facilitate $O_2^{\bullet-}$ binding.[81] Next, in the *ex vivo* model, the gene expression studies of YGQDs showed ~2.1-fold increased SOD expression levels with only 2.5 μM YGQD treatment (*i.e.*, 6-fold lower *in vitro* dose) alongwith its minimal cytotoxicity toward PBMCs and human cell lines. These preliminary results encouraged us to establish YGQDs as promising candidates for certain new SOD-dependent therapeutics to treat neural diseases.[82] In a parallel study, we also found that the progressive markers of neuronal diseases like PCO and LPO levels were normalized with lower treatment doses of YGQDs. Most importantly, the imbalance in the different release patterns of pro-inflammatory and anti-inflammatory cytokines also reverted to its normal levels with YGQDs treatment. Further, using combined confocal and phase contrast microscopy, we show that YGQDs, due to their hydrophobic and hydrophilic groups, were localized in the cytoplasm and nucleus and could protect C6-cells against apoptosis. The increased stability, cellular survival, anti-apoptotic effect, and restored cytokine release under OS estimate YGQDs as an ideal therapeutic nanozyme that can treat various neuronal disorders.

Conclusion

The present work sheds light on the step-wise establishment of biocompatible and SOD-specific YGQDs from their fabrication to neuronal stress suppression in C6-cells. The formed YGQDs were well characterized using different spectroscopic tools (like FTIR, UV, TOF-MS, XPS, Raman, and HR-TEM) and were intended for the suppression of $O_2^{\bullet-}$. *In vitro* studies proved YGQDs to be better RSA than AA, showing a dose-dependent radical quenching property. Later, the anti-oxidative role of YGQDs was reasoned for its specific SOD-like activity, determined using the enzyme activity screening. Although the YGQDs demonstrated slightly lesser kinetic control than bSOD, the YGQDs showed excellent stability over a wide range of temperatures and in the presence of strong denaturant concentrations. Furthermore, having demonstrated excellent bio-compatibility, the YGQDs, when transcribed to an *ex vivo* model, restored damaged the SOD activity at a much lower dose than the *in vitro* model. Besides its anti-oxidative roles, the YGQDs enhanced cell survivability from H_2O_2-induced cellular apoptosis. The YGQD's ability to further reverse the elevated PCO and MDA levels and simultaneously normalize the release pattern of various pro- and anti-inflammatory cytokines through cytoplasmic and nuclear internalization indicates its anti-apoptotic roles. Overall, the high anti-oxidant property and improved cellular revivability from apoptosis using YGQDs may attract future studies for treating neurodegenerative diseases, where the delivery of recombinant SOD is always a challenge. Interestingly, the pro-oxidant effect of QDs/GQDs is available from widespread synthesis. Still, the biologically important antioxidant effect with selective enzyme activity from a natural waste with high productivity is very novel and rare.

Materials and methods

General procedure and instrumentation

Sulfuric acid (H_2SO_4, 98%) (CAS: 7664-93-9), nitric acid (HNO_3, 69–72%) (CAS-7697-37-2), hydrochloric acid (HCl, 35–38% v/v) (CAS: 7647-01-0), sodium hydroxide (NaOH, 97%) (CAS: 1310-73-2), and hydrogen peroxide (H_2O_2, 30% v/v) (CAS: 7722-84-1) were purchased from Fischer scientific, India. Potassium permanganate ($KMnO_4$, extra pure grade) (CAS: 7722-64-7) was purchased from FINAR Chemicals. Double distilled water (DDW) was used for all the experimentation, and Milli-Q grade water was used for spectroscopic and adsorption analysis. Tris-EDTA buffer (SigmaAldrich) GO and YGQDs synthesized were characterized using UV-vis spectroscopy (Shimadzu, UV-1780, 200–500 nm) for determining different transitions. The functional groups, stretching, and bending vibration modes were detected using FTIR spectroscopy in working ATR (Shimadzu, IRAffinity-1S, DLATGS detector, 4000 cm^{-1} to 500 cm^{-1}). The crystallinity phases and lattice parameters were calculated using powder XRD (Rigaku Smart Lab X-ray diffractometer, 3 kW), Cu Kα radiation with a wavelength λ = 1.540 Å. The presence of longitudinal and transverse phonon modes was analyzed using micro-Raman spectroscopy (make-HORIBA scientific, Labman HR-UV-open, 500 cm^{-1} to 3000 cm^{-1}) using 532 nm laser, 1 mW power; the spectra were recorded at 50× objective. The surface morphology, lattice spacing, and EDS

composition are studied by HRTEM analysis (Thermo Scientific, Talos F200X G2, 200 kV). The emission spectra of YGQDs were recorded using a benchtop spectrofluorometer (HORIBA, Fluromax-4; 300–650 nm). Time-correlated single photon counting was measured at ε_{max} = 458 nm and 558 nm using (DeltaFlexTCSPC Lifetime Fluorimeter, 80–100 ps). XPS analysis was done using a PHI III Scanning XPS Microprobe. CHO analysis was performed using an Elementar Analysensysteme GmbH, Germany. TOF-mass was calculated using a Waters, USA XEVO G2-XS QTOF.

Synthesis of GO and YGQDs from CW

The detailed procedure for synthesizing GO from CW is mentioned in the ESI.† For YGQDs synthesis, 0.1 g GO powder was added to a pre-stirred aqueous solution of H_2O_2 : NaOH (3 : 2 mmol) to produce a final concentration of 1 mg L^{-1} at room temperature (RT). The contents were sonicated for 30 min and autoclaved at 121 °C in a polytetrafluoroethylene (PTFE)-lined bottle for 12 h. After filtering and cooling to RT, the mixture was neutralized with a 10% v/v 20 mL HCl solution. The dissolved salts were removed using a dialysis bag with a cut-off (MWCO) 3000 Da (Genaxy Pvt Ltd, Servapor dialysis membrane) for 48 h before drying at 60 °C to get pure YGQDs.

Reactive oxygen species (ROS) scavenging activity and enzyme mimetic activity of YGQDs

The radical quenching ability of YGQDs was determined using an earlier established method reported by Brand-Williams *et al.*[83] Briefly, 0.05 mL YGQDs solutions having concentrations in the range of 0–100 μM were mixed with 1.2 mL freshly prepared DPPH in 1 mM methanol solution and vortexed for 30 min. The same concentrations of AA (0–100 μM) were prepared similarly and taken as the positive control. Both solutions were then incubated in the dark for 30 min at RT. Using a UV-vis spectrophotometer, the absorbance was measured at 517 nm. The change in the color of the DPPH assay solution from purple to yellow with reduced absorbance at 517 nm indicates the scavenging activity by YGQDs and AA.

ROS determination in C6-cells by 2′,7′-dichlorodihydrofluorescein diacetate (H_2DCFDA) assay

C6-cells (1×10^6 cells per mL) were pre-mixed with YGQDs (2.5, 5, 10, and 25 μM) and then treated with H_2O_2 (200 μM) for 6 h. Untreated and H_2O_2-treated cells were taken as the negative and positive controls, respectively. These cells (2×10^6 cells per mL) were then incubated with H_2DCFDA (20 μM) for 20 min at 37 °C. ε_{max} was measured spectrofluorometrically at 530 nm at an excitation wavelength of 507 nm.

Fluorescence-activated single-cell sorting (FACS) analysis

Annexin V-FITC (AV)/propidium iodide (PI) binding of C6-cells was studied using the AV apoptosis detection kit (BD Biosciences). Briefly, YGQDs (2.5, 5, and 10 μM) pre-mixed C6-cells (1×10^6 cells per mL) were treated with H_2O_2 (200 μM) for 6 h. The cells were harvested, washed, and dissolved in 1 mL PBS, followed by mixing with the sequential addition of 5 μL PI, 20 μL binding buffer, and 5 μL AV. Following 15 min of incubation without light, cells were analyzed by a BD FACS ARIA TM Fusion flow cytometer (Becton Dickinson, CA, USA).

Data analysis was performed using BD FACSDiva 9.0.1 software.

Malondialdehyde (MDA) expression and protein carbonylation assay study

YGQDs (5, 10, and 25 μM) pre-treated C6-cells (4×10^6 cells per mL) were incubated with H_2O_2 (200 μM) for 6 h. After incubation, cells were collected and centrifuged at 7500*g* for 10 min at 4 °C. An enzyme-linked immunosorbent assay (ELISA) for MDA detection was performed using the MDA assay kit (Elabscience, Cat. no. EL-0060) as per the manufacturer's instructions. Due to redox imbalance, proteins, lipids, and nucleic acids are the major targets of ROS-mediated oxidation. The oxidative modification of the amino acids to carbonyl groups was derivatized with 2,4-dinitrophenylhydrazine (DNPH) (D199303 SigmaAldrich), followed by precipitation with 30% (w/v) trichloroacetic acid (TCA). Then, absorbance was measured at 360 nm after dissolving the DNPH-derivatized protein pellet in 1 mL 6 M guanidine HCl.

Statistical statement

The stats were analyzed by one-way and two-way analysis of variance using GraphPad Prism (version 8.00; GraphPad Software, Inc., CA, USA). The results were measured as mean ± standard deviation of at least three independent experiments. The results were shown as approximate mean values. Differences between the group data were considered statistically significant and highly significant when $p < 0.05$ and $p < 0.001$, respectively.

Note: $^*P < 0.05$; $^{**}0.05 < P < 0.01$; $^{***}0.01 < P < 0.001$.

All other methods are elaborated in the ESI.† Pretreatment of coal, Synthesis of GO from CW, HR-TEM sample preparation, UV-vis and pH study, Enzyme assay, RNA extraction, and RT-PCR, Cytotoxicity studies, H_2O_2 degradation, H_2O_2-induced damage control in Caco2 and HepG2 cells, H_2O_2 and LPS-induced damage control, ELISA (pro-inflammatory marker), YGQDs cellular uptake.

Abbreviations

Additional abbreviations

EDS	Energy dispersive X-ray spectroscopy
SAED	Selected area electron diffraction
RNA	Ribonucleic acid
M.W	Molecular weight
cDNA	Complementary DNA
PL	Photoluminescence
p-XRD	Powder X-ray diffraction
EC_{50}	Effective concentration showing 50% of activity
DPPH & DPPHH	α,α-Diphenyl-β-picrylhydrazyl
RNS	Reactive nitrogen species

FACS	Fluorescence-activated cell sorting
IFN-γ	Interferon-gamma
TNF-α	Tumor necrosis factor-alpha
IL-6 & IL-β	Interleukin chemokine
PBMC	Peripheral blood mononuclear cells
LSM	Laser scanning microscopy
FITC	Fluorescein isothiocyanate
ROS	Reactive oxygen species
RSA	Radical scavenging activity
OS	Oxidative stress
TOF	Tandem time-of-flight
MTT	(3-[4,5-Dimethylthiazol-2-yl]-2,5 diphenyl tetrazolium bromide) assay.

Author contributions

TD: conceptualization, experiments, methodology, synthesis, design, data analysis, and validation. PK: methodology, validation, and data analysis. CB: manuscript review and correction, data validation, and supervision. DM: conceptualization, methodology, review, and manuscript editing. SD: supervision, manuscript review and editing, data validation, conceptualization.

Conflicts of interest

All the authors declare that there is no competing financial interest involved.

Acknowledgements

BRNS (54/14/15/2020-BRNS/35054). All the authors have contributed and acknowledged BRNS for providing funds for carrying out the work and the National Institute of Technology Patna and National Institute of Pharmaceutical Education and Research Hajipur for providing laboratory aid and other instrumentation facilities. All the authors thank the Central research facilities at IIT (ISM) Dhanbad and IIT Mumbai for providing advanced analysis. We also acknowledge Dr. S. K. Sahu, IIT (ISM) Dhanbad and Dr. C. Bora, Patna Science College, Patna for their suggestions. Finally, all the other anonymous reviewers are thanked for their valuable comments towards making this a successful contribution.

References

1 Y. Volkov, *Biochem. Biophys. Res. Commun.*, 2015, **468**, 419–427.
2 L. Lin and S. Zhang, *ChemComm*, 2012, **48**, 10177.
3 D. B. Shinde and V. K. Pillai, *Chem. – Eur. J.*, 2012, **18**, 12522–12528.
4 Y. Dong, H. Pang, S. Ren, C. Chen, Y. Chi and T. Yu, *Carbon*, 2013, **64**, 245–251.
5 D. Torres, J. L. Pinilla, E. M. Gálvez and I. Suelves, *RSC Adv.*, 2016, **6**, 48504–48514.
6 W. Wang, Z. Wang, J. Liu, Y. Peng, X. Yu, W. Wang, Z. Zhang and L. Sun, *Ind. Eng. Chem. Res.*, 2018, **57**, 9144–9150.
7 Z. Wang, J. Yu, X. Zhang, N. Li, B. Liu, Y. Li, Y. Wang, W. Wang, Y. Li, L. Zhang, S. Dissanayake, S. L. Suib and L. Sun, *ACS Appl. Mater. Interfaces*, 2016, **8**, 1434–1439.
8 A. Abbas, L. T. Mariana and A. N. Phan, *Carbon*, 2018, **140**, 77–99.
9 M. He, X. Guo, J. Huang, H. Shen, Q. Zeng and L. Wang, *Carbon*, 2018, **140**, 508–520.
10 S. P. Sasikala, L. Henry, G. Yesilbag Tonga, K. Huang, R. Das, B. Giroire, S. Marre, V. M. Rotello, A. Penicaud, P. Poulin and C. Aymonier, *ACS Nano*, 2016, **10**, 5293–5303.
11 S. Kang, K. M. Kim, K. Jung, Y. Son, S. Mhin, J. H. Ryu, K. B. Shim, B. Lee, H. S. Han and T. Song, *Sci. Rep.*, 2019, **9**, 4101.
12 Y. Liu, B. Gao, Z. Qiao, Y. Hu, W. Zheng, L. Zhang, Y. Zhou, G. Ji and G. Yang, *Chem. Mater.*, 2015, **27**, 4319–4327.
13 A. Abbas, T. A. Tabish, S. J. Bull, T. M. Lim and A. N. Phan, *Sci. Rep.*, 2020, **10**, 21262.
14 R. Ye, C. Xiang, J. Lin, Z. Peng, K. Huang, Z. Yan, N. P. Cook, E. L. G. Samuel, C.-C. Hwang, G. Ruan, G. Ceriotti, A.-R. O. Raji, A. A. Martí and J. M. Tour, *Nat. Commun.*, 2013, **4**, 2943.
15 Q. Liu, J. Zhang, H. He, G. Huang, B. Xing, J. Jia and C. Zhang, *Nanomaterials*, 2018, **8**, 844.
16 Y. Zhang, K. Li, S. Ren, Y. Dang, G. Liu, R. Zhang, K. Zhang, X. Long and K. Jia, *ACS Sustainable Chem. Eng.*, 2019, **7**, 9793–9799.
17 A. Kundu, B. Maity and S. Basu, *New J. Chem.*, 2022, **46**, 7545–7556.
18 Y. Dong, J. Lin, Y. Chen, F. Fu, Y. Chi and G. Chen, *Nanoscale*, 2014, **6**, 7410–7415.
19 N. Morimoto, T. Kubo and Y. Nishina, *Sci. Rep.*, 2016, **6**, 21715.
20 A. D. Lemly, *Hum Ecol. Risk. Assess.*, 2017, **24**, 627–641.
21 K. M. Zierold and C. Odoh, *Rev. Environ. Health*, 2020, **35**, 401–418.
22 M. Whiteside and J. Herndon, *J. Adv. Med. Med. Res.*, 2018, **25**, 1–11.
23 S. Chung, R. A. Revia and M. Zhang, *Adv. Mater.*, 2019, **33**, 1904362.
24 H. Wang, C. Liu, Z. Liu, J. Ren and X. Qu, *Small*, 2018, **14**, 1703710.
25 H. Sun, A. Zhao, N. Gao, K. Li, J. Ren and X. Qu, *Angew. Chem., Int. Ed.*, 2015, **54**, 7176–7180.
26 Y. Lin, L. Wu, Y. Huang, J. Ren and X. Qu, *Chem. Sci.*, 2015, **6**, 1272–1276.
27 H. Sun, Y. Zhou, J. Ren and X. Qu, *Angew. Chem., Int. Ed.*, 2018, **57**, 9224–9237.
28 A. Sun, L. Mu and X. Hu, *ACS Appl. Mater. Interfaces*, 2017, **9**, 12241–12252.
29 D. Kim, J. M. Yoo, H. Hwang, J. Lee, S. H. Lee, S. P. Yun, M. J. Park, M. J. Lee, S. Choi, S. H. Kwon, S. Lee,

S.-H. Kwon, S. Kim, Y. J. Park, M. Kinoshita, Y.-H. Lee, S. Shin, S. R. Paik, S. J. Lee, S. Lee, B. H. Hong and H. S. Ko, *Nat. Nanotechnol.*, 2018, **13**, 812–818.
30 L. Hu, W. Sun, Y. Tang, S. Li, B. Zhang, X. Sun, W. Ji, L. Ma, H. Deng, S. Han and D. Zhu, *Carbon*, 2021, **176**, 148–156.
31 Q. Xin, X. Jia, A. Nawaz, W. Xie, L. Li and J. R. Gong, *Nano Res.*, 2020, **13**, 1427–1433.
32 H. Sun, A. Zhao, N. Gao, K. Li, J. Ren and X. Qu, *Angew. Chem., Int. Ed.*, 2015, **54**, 7176–7180.
33 N. R. Nirala, G. Khandelwal, B. Kumar, Vinita, R. Prakash and V. Kumar, *Talanta*, 2017, **173**, 36–43.
34 Y. Wang, W. Kong, L. Wang, J. Z. Zhang, Y. Li, X. Liu and Y. Li, *Phys. Chem. Chem. Phys.*, 2019, **21**, 1336–1343.
35 L. Nilewski, K. Mendoza, A. S. Jalilov, V. Berka, G. Wu, W. K. Sikkema, A. Metzger, R. Ye, R. Zhang, D. X. Luong, T. Wang, E. McHugh, P. J. Derry, E. L. Samuel, T. A. Kent, A.-L. Tsai and J. M. Tour, *ACS Appl. Mater. Interfaces*, 2019, **11**, 16815–16821.
36 M. Krunić, B. Ristić, M. Bošnjak, V. Paunović, G. Tovilović-Kovačević, N. Zogović, A. Mirčić, Z. Marković, B. Todorović-Marković, S. Jovanović, D. Kleut, M. Mojović, Đ. Nakarada, O. Marković, I. Vuković, L. Harhaji-Trajković and V. Trajković, *Free Radicals Biol. Med.*, 2021, **177**, 167–180.
37 L. Wang, Y. Li, Y. Wang, W. Kong, Q. Lu, X. Liu, D. Zhang and L. Qu, *ACS Appl. Mater. Interfaces*, 2019, **11**, 21822–21829.
38 V. L. Feigin, T. Vos, E. Nichols, M. O. Owolabi, W. M. Carroll, M. Dichgans, G. Deuschl, P. Parmar, M. Brainin and C. Murray, *Lancet Neurol.*, 2020, **19**, 255–265.
39 N. Khatri, M. Thakur, V. Pareek, S. Kumar, S. Sharma and A. K. Datusalia, *CNS Neurol. Disord. Drug Targets*, 2018, **17**, 689–695.
40 J. P. Bolaños, M. A. Moro, I. Lizasoain and A. Almeida, *Adv. Drug Delivery Rev.*, 2009, **61**, 1299–1315.
41 B. Uttara, A. Singh, P. Zamboni and R. Mahajan, *Curr. Neuropharmacol.*, 2009, **7**, 65–74.
42 Y. Gilgun-Sherki, E. Melamed and D. Offen, *Neuropharmacology*, 2001, **40**, 959–975.
43 C. Ren, X. Hu and Q. Zhou, *Adv. Sci.*, 2018, **5**, 1700595.
44 O. M. Ighodaro and O. A. Akinloye, *Alexandria J. Med.*, 2018, **54**, 287–293.
45 (*a*) D. C. Marcano, D. V. Kosynkin, J. M. Berlin, A. Sinitskii, Z. Sun, A. Slesarev, L. B. Alemany, W. Lu and J. M. Tour, *ACS Nano*, 2010, **4**, 4806–4814; (*b*) P. Kumar, B. Yadav, A. Kumar, C. Bora, A. Kumar and S. Das, *FlatChem*, 2021, **27**, 100245.
46 Y. Zhao, X. Wu, S. Sun, L. Ma, L. Zhang and H. Lin, *Carbon*, 2017, **124**, 342–347.
47 U. Stoin, A. I. Shames, I. Malka, I. Bar and Y. Sasson, *ChemPhysChem*, 2013, **14**, 4158–4164.
48 G.-L. Hong, H.-L. Zhao, H.-H. Deng, H.-J. Yang, H.-P. Peng, Y.-H. Liu and W. Chen, *Int. J. Nanomed.*, 2018, **13**, 4807–4815.
49 F. Liu, M.-H. Jang, H. D. Ha, J.-H. Kim, Y.-H. Cho and T. S. Seo, *Adv. Mater.*, 2013, **25**, 3657–3662.
50 G. Venugopal, M.-H. Jung, M. Suemitsu and S.-J. Kim, *Carbon*, 2011, **49**, 2766–2772.
51 T. Livneh, T. L. Haslett and M. Moskovits, *Phys. Rev. B*, 2002, **66**, 195110.
52 Y. Li, Y. Hu, Y. Zhao, G. Shi, L. Deng, Y. Hou and L. Qu, *Adv. Mater.*, 2010, **23**, 776–780.
53 (*a*) C. Hontoria-Lucas, A. J. López-Peinado, J. D. López-González, M. L. Rojas-Cervantes and R. M. Martín-Aranda, *Carbon*, 1995, **33**, 1585–1592; (*b*) P. Kumar, C. Bora, B. Kumar, P. Kr. Sukul and S. Das, *Synth. Met.*, 2020, **264**, 116381.
54 K. He, N. Chen, C. Wang, L. Wei and J. Chen, *Cryst. Res. Technol.*, 2018, **53**, 1700157.
55 B. D. Cullity and J. W. Weymouth, *Am. J. Phys.*, 1957, **25**, 394–395.
56 Y. Dong, H. Pang, H. B. Yang, C. Guo, J. Shao, Y. Chi, C. M. Li and T. Yu, *Angew. Chem., Int. Ed.*, 2013, **52**, 7800–7804.
57 S. Ahirwar, S. Mallick and D. Bahadur, *ACS Omega*, 2017, **2**, 8343–8353.
58 Y. Chong, C. Ge, G. Fang, X. Tian, X. Ma, T. Wen, W. G. Wamer, C. Chen, Z. Chai and J.-J. Yin, *ACS Nano*, 2016, **10**, 8690–8699.
59 B. Kong, T. Yang, F. Cheng, Y. Qian, C. Li, L. Zhan, Y. Li, H. Zou and C. Huang, *J. Colloid Interface Sci.*, 2022, **611**, 545–553.
60 B.-C. Lee, J. Y. Lee, J. Kim, J. M. Yoo, I. Kang, J.-J. Kim, N. Shin, D. J. Kim, S. W. Choi, D. Kim, B. H. Hong and K.-S. Kang, *Sci. Adv.*, 2020, **6**, eaaz2630.
61 L. Wang, Y. Li, L. Zhao, Z. Qi, J. Gou, S. Zhang and J. Z. Zhang, *Nanoscale*, 2020, **12**, 19516–19535.
62 P. Kumar, P. Shivam, S. Mandal, P. Prasanna, S. Kumar, S. R. Prasad, A. Kumar, P. Das, V. Ali, S. K. Singh and D. Mandal, *Int. J. Nanomed.*, 2019, **14**, 6073–6101.
63 J. Zhao, W. Gao, X. Cai, J. Xu, D. Zou, Z. Li, B. Hu and Y. Zheng, *Theranostics*, 2019, **9**, 2843–2855.
64 X. Wang, H. Wang and S. Zhou, *J. Phys. Chem. Lett.*, 2021, **12**, 11751–11760.
65 M. Hassan, E. Haque, K. R. Reddy, A. I. Minett, J. Chen and V. G. Gomes, *Nanoscale*, 2014, **6**, 11988–11994.
66 S. Arunragsa, Y. Seekaew, W. Pon-On and C. Wongchoosuk, *Diamond Relat. Mater.*, 2020, **105**, 107790.
67 A. S. Jalilov, L. G. Nilewski, V. Berka, C. Zhang, A. A. Yakovenko, G. Wu, T. A. Kent, A.-L. Tsai and J. M. Tour, *ACS Nano*, 2017, **11**, 2024–2032.
68 R. Yuan, Y. Li, S. Han, X. Chen, J. Chen, J. He, H. Gao, Y. Yang, S. Yang and Y. Yang, *ACS Cent. Sci.*, 2021, **8**, 10–21.
69 A. Quincozes-Santos, L. D. Bobermin, A. Latini, M. Wajner, D. O. Souza, C.-A. Gonçalves and C. Gottfried, *PLoS One*, 2013, **8**, 64372.
70 H. Guo, H. Guo, Y. Xie, Y. Chen, C. Lu, Z. Yang, Y. Zhu, Y. Ouyang, Y. Zhang and X. Wang, *Redox Biol.*, 2022, **56**, 102441.
71 R. Omar, M. Smith, G. Perry and M. Pappolla, *J. Neuropathol. Exp. Neurol.*, 1996, **55**, 634.

72 F. P. Zemlan, O. J. Thienhaus and H. B. Bosmann, *Brain Res.*, 1989, **476**, 160–162.
73 D. W. Cleveland and J. D. Rothstein, *Nat. Rev. Neurosci.*, 2001, **2**, 806–819.
74 J. Choi, H. D. Rees, S. T. Weintraub, A. I. Levey, L.-S. Chin and L. Li, *J. Biol. Chem.*, 2005, **280**, 11648–11655.
75 C. A. Massaad, T. M. Washington, R. G. Pautler and E. Klann, *Proc. Natl. Acad. Sci. U. S. A.*, 2009, **106**, 13576–13581.
76 B. Mansuroğlu, S. Derman, A. Yaba and K. Kızılbey, *Int. J. Biol. Macromol.*, 2015, **72**, 79–87.
77 A. Azari, R. Nabizadeh, S. Nasseri, A. H. Mahvi and A. R. Mesdaghinia, *Chemosphere*, 2020, **250**, 126238.
78 S. Mandal, S. R. Prasad, D. Mandal and P. Das, *ACS Appl. Mater. Interfaces*, 2019, **11**, 33273–33284.
79 S. Nayak, S. R. Prasad, D. Mandal and P. Das, *J. Hazard. Mater.*, 2020, **392**, 122287.
80 B. A. Al Jahdaly, M. F. Elsadek, B. M. Ahmed, M. F. Farahat, M. M. Taher and A. M. Khalil, *Sustainability*, 2021, **13**, 2127.
81 W. Gao, J. He, L. Chen, X. Meng, Y. Ma, L. Cheng, K. Tu, X. Gao, C. Liu, M. Zhang, K. Fan, D.-W. Pang and X. Yan, *Nat. Commun.*, 2023, **14**, 160.
82 P. Saxena, K. Selvaraj, S. K. Khare and N. Chaudhary, *Biotechnol. Lett.*, 2021, **44**, 1–22.
83 W. Brand-Williams, M. E. Cuvelier and C. Berset, *LWT–Food Sci. Technol.*, 1995, **28**, 25–30.